



Article

Cr³⁺ Doping Effects on Structural, Optical, and Morphological Characteristics of BaTiO₃ Nanoparticles and Their Bioactive Behavior

Efracio Mamani Flores ¹, Bertha Silvana Vera Barrios ^{2,*}, Julio César Huillca Huillca ¹, Jesús Alfredo Chacaltana García ¹, Carlos Armando Polo Bravo ¹, Henry Edgardo Nina Mendoza ¹, Alberto Bacilio Quispe Cohaila ^{3,4}, Francisco Gamarra Gómez ⁵, Rocío María Tamayo Calderón ⁶, Gabriela de Lourdes Fora Quispe ^{4,7} and Elisban Juani Sacari Sacari ^{4,8,*}

- ¹ Departamento de Física Aplicada, Facultad de Ciencias, Universidad Nacional Jorge Basadre Grohmann, Avenida Miraflores S/N, Ciudad Universitaria, Tacna 23003, Peru
 - ² Facultad Ing. de Minas, Universidad Nacional de Moquegua, Moquegua 18001, Peru
 - ³ Laboratorio de Generación y Almacenamiento de Hidrogeno, Facultad de Ingeniería, Universidad Nacional Jorge Basadre Grohmann, Avenida Miraflores S/N, Ciudad Universitaria, Tacna 23003, Peru
 - ⁴ Grupo de Investigación GIMAEC, Facultad de Ingeniería, Universidad Nacional Jorge Basadre Grohmann, Avenida Miraflores S/N, Ciudad Universitaria, Tacna 23003, Peru
 - ⁵ Laboratorio de Nanotecnología, Facultad de Ingeniería, Universidad Nacional Jorge Basadre Grohmann, Avenida Miraflores S/N, Ciudad Universitaria, Tacna 23003, Peru
 - ⁶ Centro de Microscopia Electrónica, Facultad de Ingeniería de Procesos, Universidad Nacional de San Agustín, Arequipa 04001, Peru
 - ⁷ Laboratorio de Biorremediación, Facultad de Ciencias, Universidad Nacional Jorge Basadre Grohmann, Avenida Miraflores S/N, Ciudad Universitaria, Tacna 23003, Peru
 - ⁸ Facultad de Ciencias, Universidad Nacional de Ingeniería, Av. Túpac Amaru 210, Lima 15333, Peru
- * Correspondence: anavlisarev@gmail.com (B.S.V.B.); esacaris@unjbg.edu.pe (E.J.S.S.); Tel.: +51-925573684 (E.J.S.S.)



Citation: Mamani Flores, E.; Vera Barrios, B.S.; Huillca Huillca, J.C.; Chacaltana García, J.A.; Polo Bravo, C.A.; Nina Mendoza, H.E.; Quispe Cohaila, A.B.; Gamarra Gómez, F.; Tamayo Calderón, R.M.; Fora Quispe, G.d.L.; et al. Cr³⁺ Doping Effects on Structural, Optical, and Morphological Characteristics of BaTiO₃ Nanoparticles and Their Bioactive Behavior. *Crystals* **2024**, *14*, 998. <https://doi.org/10.3390/cryst14110998>

Academic Editors: Adriana-Gabriela Schiopu and Laura Madalina Cursaru

Received: 9 August 2024

Revised: 16 November 2024

Accepted: 17 November 2024

Published: 19 November 2024



Copyright: © 2024 by the authors. Licensee MDPI, Basel, Switzerland. This article is an open access article distributed under the terms and conditions of the Creative Commons Attribution (CC BY) license (<https://creativecommons.org/licenses/by/4.0/>).

Abstract: This study investigates the effects of chromium (Cr³⁺) doping on BaTiO₃ nanoparticles synthesized via the sol–gel route. X-ray diffraction confirms a Cr-induced cubic-to-tetragonal phase transition, with lattice parameters and crystallite size varying systematically with Cr³⁺ content. UV–visible spectroscopy reveals a monotonic decrease in bandgap energy from 3.168 eV (pure BaTiO₃) to 2.604 eV (5% Cr³⁺-doped BaTiO₃). Raman and FTIR spectroscopy elucidate structural distortions and vibrational mode alterations caused by Cr³⁺ incorporation. Transmission electron microscopy and energy-dispersive X-ray spectroscopy verify nanoscale morphology and successful Cr³⁺ doping (up to 1.64 atom%). Antioxidant activity, evaluated using the DPPH assay, shows stable radical scavenging for pure BaTiO₃ (40.70–43.33%), with decreased activity at higher Cr³⁺ doping levels. Antibacterial efficacy against *Escherichia coli* peaks at 0.5% Cr³⁺ doping (10.569 mm inhibition zone at 1.5 mg/mL), decreasing at higher concentrations. This study demonstrates the tunability of structural, optical, and bioactive properties in Cr³⁺-doped BaTiO₃ nanoparticles, highlighting their potential as multifunctional materials for electronics, photocatalysis, and biomedical applications.

Keywords: BaTiO₃; sol–gel; doping; phase change and bioactive

1. Introduction

Barium titanate (BaTiO₃) nanoparticles have garnered significant attention in materials science due to their exceptional ferroelectric, piezoelectric, and dielectric properties [1,2]. These nanoparticles, belonging to the perovskite family with the general formula ABO₃ [3], exhibit a unique crystal structure that undergoes several phase transitions, each associated with distinct functional characteristics. At the nanoscale, BaTiO₃ exhibits distinct advantages over its bulk counterpart. Nanoparticles with diameters below 100 nm show a reduced Curie temperature of 30–50 °C compared to bulk, extending their ferroelectric

behavior to lower temperatures [4,5]. The dielectric constant increases significantly, with values up to 15,000 reported for 70 nm particles, enhancing capacitor performance [6]. Piezoelectric coefficients are also amplified, with a d_{33} of 416 pC/N observed in 100 nm BaTiO₃, compared to 216 pC/N in 500 nm particles [7]. Additionally, the surface area can increase up to seven times with the reduction of particle size from 70 nm to 10 nm, which can enhance the catalytic activity [8]. These quantifiable nanoscale-specific properties make BaTiO₃ nanoparticles promising for applications in miniaturized electronics, high-sensitivity sensors, and efficient photocatalysts [2].

Various synthesis methods have been employed to produce BaTiO₃ nanoparticles, each offering distinct advantages and challenges. Conventional solid-state reactions, while straightforward, often require high temperatures and yield particles with limited size control [9]. Coprecipitation methods allow for lower processing temperatures but can struggle with precise stoichiometry control [10]. Hydrothermal synthesis offers good control over particle morphology and size, but is limited by small production volumes due to high-pressure autoclave reactors [11]. Other methods such as microwave-assisted and combustion synthesis have also been investigated [12,13]. Among these techniques, the sol-gel method stands out for its versatility and effectiveness in producing high-quality BaTiO₃ nanoparticles [14], particularly when incorporating dopants. This method involves the transition of a system from a colloidal suspension (sol) into a three-dimensional network structure that entraps the solvent (gel), allowing for molecular-level mixing of the precursors and dopants. The gel state, an intermediate phase in this process, plays a crucial role in controlling the evolution of the material, enabling precise tailoring of the composition, particle size, and morphology [15]. Furthermore, the sol-gel approach facilitates homogeneous dopant distribution and allows for the synthesis of nanocrystalline materials at relatively low temperatures [16], making it particularly suitable for studying the effects of dopant incorporation on BaTiO₃ properties.

The incorporation of dopants into the BaTiO₃ lattice has emerged as a powerful strategy to further tailor its properties [17]. Among various dopants, trivalent chromium (Cr³⁺) has shown particular promise due to its ability to simultaneously modulate the structural, optical, and electrical properties of BaTiO₃ nanoparticles. The ionic radius of Cr³⁺ (0.69 Å) closely matches that of Ti⁴⁺ (0.68 Å), facilitating its substitution at the B-site of the perovskite structure [18]. This substitution introduces complex defect chemistry, profoundly affecting the characteristics of the material at multiple scales.

From a structural perspective, Cr³⁺ doping induces lattice distortions and alters the phase transition behavior of BaTiO₃ nanoparticles [19]. These structural modifications can significantly influence the material's ferroelectric and piezoelectric responses, potentially enhancing its performance in various applications [20]. The precise control over the crystal structure through Cr³⁺ doping offers a unique opportunity to tailor the functional properties of BaTiO₃ nanoparticles for specific technological needs.

The optical properties of BaTiO₃ nanoparticles undergo substantial changes upon Cr³⁺ doping. The introduction of Cr³⁺ ions creates additional electronic states within the bandgap, leading to a reduction in the optical bandgap energy [21]. This bandgap engineering not only alters the optical absorption characteristics of the material, resulting in visible color changes, but also expands its potential for photocatalytic and optoelectronic applications [22]. The ability to tune the optical absorption characteristics through Cr³⁺ doping opens up new avenues for utilizing BaTiO₃ nanoparticles in light-driven technologies.

Morphologically, Cr³⁺ doping can significantly influence the size, shape, and surface properties of BaTiO₃ nanoparticles [23,24]. These morphological changes are crucial as they directly impact the material's reactivity, catalytic activity, and interaction with its environment. Understanding and controlling the morphological evolution of Cr³⁺-doped BaTiO₃ nanoparticles is essential for optimizing their performance in various applications, particularly those involving interface-dependent processes [25].

Perhaps most intriguingly, recent research has hinted at the potential bioactive behavior of Cr³⁺-doped BaTiO₃ nanoparticles, opening up exciting possibilities in the realm

of biomedical applications [3]. The unique combination of ferroelectric properties and controlled doping may impart novel functionalities relevant to biological interactions [26]. These could include enhanced biocompatibility, antimicrobial activity, or the ability to influence cellular processes through localized charge distributions or piezoelectric effects [27].

This study aims to provide a comprehensive investigation of the effects of Cr³⁺ doping on the structural, optical, and morphological characteristics of BaTiO₃ nanoparticles, with a particular focus on their resultant bioactive behavior. Using advanced characterization techniques, we aim to unravel the complex relationships between doping concentration, nanoparticle characteristics, and biological interactions. This research contributes to the fundamental understanding of doped ferroelectric nanomaterials but also paves the way for their rational design in next-generation applications in biomedicine.

2. Materials and Methods

2.1. Materials

High-purity analytical grade materials were used for the preparation of pure and Cr³⁺-doped barium titanate, including barium nitrate (Ba[NO₃]₂, Merck, 99.0%), titanium (IV) isopropoxide (C₁₂H₂₈O₄Ti, Sigma Aldrich, 97%, St. Louis, MO, USA), chromium (III) nitrate nonahydrate (CrN₃O₉·9H₂O, Sigma Aldrich, 99%, MO, USA), citric acid (C₆H₈O₇, Sigma Aldrich, MO, USA), 2-propanol (CH₃CH[OH]CH₃, Merck, Darmstadt, Germany), DPPH (2,2-Difenil-1-(2,4,6-trinitrofenil)hidrazil, Merck Darmstadt, Germany), Mueller–Hinton agar (Merck Darmstadt, Germany), and ultrapure water.

2.2. Pure and Cr³⁺-Doped BaTiO₃ Synthesis

The sol–gel method was employed for synthesizing pure and Cr³⁺-doped BaTiO₃ nanoparticles. This method was chosen for its ability to achieve molecular-level mixing of the precursors and dopants, facilitating homogeneous composition and precise control over the doping process.

Ultrapure water (20 mL) was used to dissolve barium nitrate (6.25 mmol), while 2-propanol served in two steps: 5 mL to dissolve citric acid (1.7 mmol) and another 5 mL for titanium isopropoxide (6.25 mmol). For Cr³⁺-doping, barium nitrate was partially substituted with chromium nitrate (0.03, 0.05, 0.1, 0.3, and 0.5 mol%). These solutions were prepared separately and combined sequentially, with the barium nitrate and citric acid solutions mixed and stirred for 150 min before the dropwise addition of the titanium isopropoxide solution. The gel state, characterized by a three-dimensional network structure entrapping the solvent, is crucial in this process. It allows for the homogeneous distribution of dopants at the molecular level, particularly important for achieving uniform Cr³⁺ incorporation into the BaTiO₃ lattice. This stage significantly influences the final properties of the material.

Gels underwent aging at 50 °C for 12 h, during which further condensation reactions and structural reorganization occurred. The dried gels were ground into fine powders and thermally treated at 700 °C for two hours, causing gel network breakdown, organic component removal, and BaTiO₃ phase crystallization.

2.3. Characterization

A comprehensive array of analytical techniques was utilized to characterize the structural, compositional, thermal, optical, vibrational, and morphological properties of pure and chromium-doped barium titanate (BaTiO₃) ceramic samples. Simultaneous thermogravimetric analysis and differential scanning calorimetry were conducted on the dried gel precursors prior to calcination using an SDT 650 module from TA Instruments (New Castle, DE, USA) to study the thermal decomposition behavior of the precursors, determine the optimal calcination temperature for crystalline BaTiO₃ formation, and quantify changes in thermal behavior and weight loss. The samples were heated from room temperature to 900 °C at a constant rate of 20 °C per minute under a nitrogen atmosphere. X-ray diffraction patterns were collected using a PANalytical Aeris diffractometer (PANalytical, Almelo,

The Netherlands) with copper K-alpha radiation and a nickel filter, and Rietveld refinement of the patterns enabled the determination of the crystal structure and crystallite size. Additionally, vibrational spectroscopy based on a 532 nm Raman microscope from Ocean Optics (MAYA 2000-Pro, Ocean Optics, Dunedin, FL, USA) was utilized to acquire Raman spectra. Diffuse reflectance spectroscopy in the ultraviolet–visible wavelength range was performed using an Evolution 220 spectrometer from Thermo Scientific (San Jose, CA, USA). Infrared spectroscopy was performed on a Bruker Invenio R Fourier Transform Infrared spectrometer equipped with an attenuated total reflectance accessory (Bruker, Saarbrücken, Germany). Photoluminescence spectra were recorded using a Fluoromax Plus spectrometer (Horiba Scientific, Irvine, CA, USA). The morphology and microstructure were evaluated using transmission electron microscopy on a Thermo Scientific Talos F200i microscope (Thermo Scientific Co., Eindhoven, The Netherlands).

2.4. Antioxidant Activity

Pure and doped Barium titanate nanoparticle solutions were prepared at varying concentrations ranging from 0.5 to 4 mg/mL. The radical scavenging activity was assessed by reacting the BaTiO₃ nanoparticles solutions with the stable free radical 2,2-diphenyl-1-picrylhydrazyl (DPPH). Specifically, 50 µL of each sample concentration was added in triplicate to the wells of a 96-well microplate followed by the addition of a 50 µL methanolic solution of 100 µM DPPH. Control wells contained 50 µL DPPH solution and 50 µL sterile deionized water. The microplate was incubated at room temperature in the dark for 20 min. Thereafter, the absorbance was measured at 517 nm using a spectrophotometer (Epoch 2C, Biotek Instruments, Winooski, VT, USA). The assays were performed in three independent replicates. Radical scavenging percentages were computed using the following equation:

$$\text{Percent scavenging (\%)} = \frac{A_0 - A_1}{A_0} \cdot 100$$

where A_0 = absorbance of DPPH control and A_1 = absorbance of DPPH solution after reaction with the pure and doped BaTiO₃ nanoparticles.

2.5. Antibacterial Activity Assay

The antimicrobial activity of pure and doped BaTiO₃ nanoparticles was evaluated against *E. coli* using the Kirby–Bauer disk diffusion method. *E. coli* was cultured in Mueller–Hinton broth at 37 °C for 24 h prior to use on agar plates. *E. coli* inoculum was prepared by adjusting the turbidity to match the 0.5 McFarland standard, corresponding to an approximate cell density of 1.5×10^8 CFU/mL. Mueller–Hinton agar plates were inoculated with 100 µL of bacterial suspension evenly spread across the surface. Sterile filter paper discs (6 mm diameter) (Oxoid Ltd., Basingstoke, UK) were prepared from deactivated sensitivity test discs through a validated sterilization protocol (autoclaving at 121 °C for 15 min in distilled water, followed by triple rinsing with sterile distilled water and dry heat sterilization at 180 °C for 1 h). Complete deactivation was verified through control experiments. These blank discs were then impregnated with varying concentrations of pure and doped BaTiO₃ nanoparticle suspensions (0.5–4 mg/mL). The impregnated discs were dried at room temperature under sterile conditions before being placed on the inoculated agar plates. BaTiO₃ nanoparticle solutions were prepared in sterile deionized water. The agar plates were incubated at 37 °C for 24 h under aerobic conditions. Deionized water was used as a negative control in parallel with all antibacterial experiments. The negative control experiments were conducted under identical conditions to those used for testing the Cr³⁺-doped BaTiO₃ nanoparticles.

Finally, the diameters of the inhibition zones formed around the disks were measured to evaluate the antimicrobial activity. The assays were performed in triplicate and the mean inhibition zone diameters were recorded for each BaTiO₃ nanoparticle concentration.

3. Results and Discussion

3.1. Thermal Analysis

Thermogravimetric analysis (TGA) and differential scanning calorimetry (DSC) were employed to investigate the thermal behavior of pure and Cr³⁺-doped BaTiO₃ nanoparticles synthesized using citric acid as the chelating agent (Figure 1). The TGA curves (Figure 1a) reveal varied weight loss patterns across the doping concentrations. Notably, the 5% Cr³⁺-doped sample exhibits a higher mass loss compared to the undoped sample, suggesting that Cr³⁺ doping has a complex effect on the thermal behavior of BaTiO₃ nanoparticles. This may involve influencing the retention of volatile species or altering decomposition pathways of residual organics, particularly the citric acid chelate complexes [28,29].

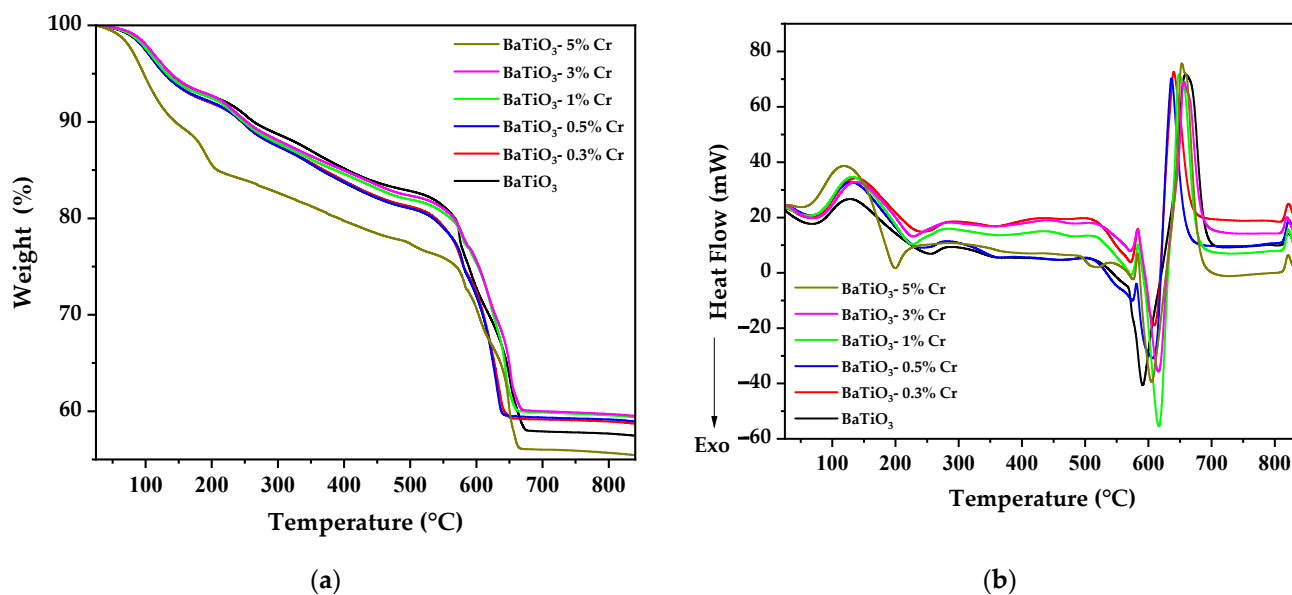


Figure 1. (a) Thermogravimetric analysis and (b) differential scanning calorimetry of pure and Cr³⁺-doped BaTiO₃.

The DSC curves (Figure 1b) provide insight into the energetic processes occurring during heating. An endothermic event around 100 °C is primarily attributed to the evaporation of residual moisture. The subsequent thermal events in the 200–500 °C range correspond to a complex series of decomposition processes, primarily involving the citric acid used as the chelating agent in our synthesis [30]. Citric acid decomposition typically occurs over a broad temperature range (177–500 °C) [31], which aligns with our observations. The exothermic nature of these events suggests the combustion of organic material, releasing energy that may facilitate the initial stages of BaTiO₃ formation.

The exothermic peak observed around 600 °C corresponds to the crystallization of BaTiO₃. Interestingly, the peak temperatures for Cr³⁺-doped samples are slightly higher than the undoped sample, suggesting that Cr³⁺ doping may increase the energy required for crystallization. This could be due to lattice distortions, altered nucleation dynamics, or the influence of Cr³⁺ on the decomposition products of the citric acid complexes [28,32].

The role of Cr³⁺ in the crystallization and phase transition of BaTiO₃ is complex. While Cr³⁺ doping appears to slightly increase the crystallization temperature, it may still influence the subsequent cubic-to-tetragonal transition. Recent studies have shown that transition metal dopants can create local distortions in the BaTiO₃ lattice, potentially serving as nucleation points for the tetragonal phase [33–35]. However, this transition is not distinctly visible in our DSC data, likely due to the small energy difference between the cubic and tetragonal phases in nanocrystalline BaTiO₃. The exact mechanism in our Cr³⁺-doped samples requires further investigation, potentially using in situ diffraction techniques to resolve the subtle structural changes during heating.

The varied weight loss patterns observed in TGA, particularly for higher Cr^{3+} doping levels, may be attributed to the formation of different metal–citrate complexes during synthesis. These complexes could have different thermal stabilities and decomposition pathways, leading to the observed variations in weight loss. This complex interplay between Cr^{3+} doping, citric acid complexation, and thermal decomposition underscores the intricate nature of the synthesis–structure–property relationships in these doped nanoparticles.

3.2. X-Ray Diffraction

The X-ray diffraction (XRD) patterns are shown in Figure 2a. The analysis reveals the influence of chromium (Cr^{3+}) doping on the structural transformation of BaTiO_3 , where Cr^{3+} was introduced through chromium nitrate dissolved in 2-propanol during the sol–gel synthesis. The pristine BaTiO_3 exhibits a cubic crystal system (Pm-3m space group), characterized by a single peak in the XRD pattern at $2\theta \approx 45.75^\circ$ (Figure 2b). The observed XRD pattern for the cubic phase shows good agreement with the reference pattern (Figure S1) from the Crystallography Open Database [36] (COD 96-591-0150). Upon Cr^{3+} doping at the A site through the controlled substitution of Ba^{2+} during the sol–gel process, a structural transition to the tetragonal phase (P4mm space group) is observed (Figure 2b), evidenced by the splitting of the original peak into a doublet, with a new shoulder appearing at $2\theta \approx 45.25^\circ$ for Cr^{3+} -doped samples. The XRD pattern of the Cr^{3+} -doped samples matches well with the COD entry 96-152-5438, indicating the successful formation of the tetragonal phase. These findings are consistent with the well-established concept of dopant-induced phase transitions in perovskite oxides [37,38].

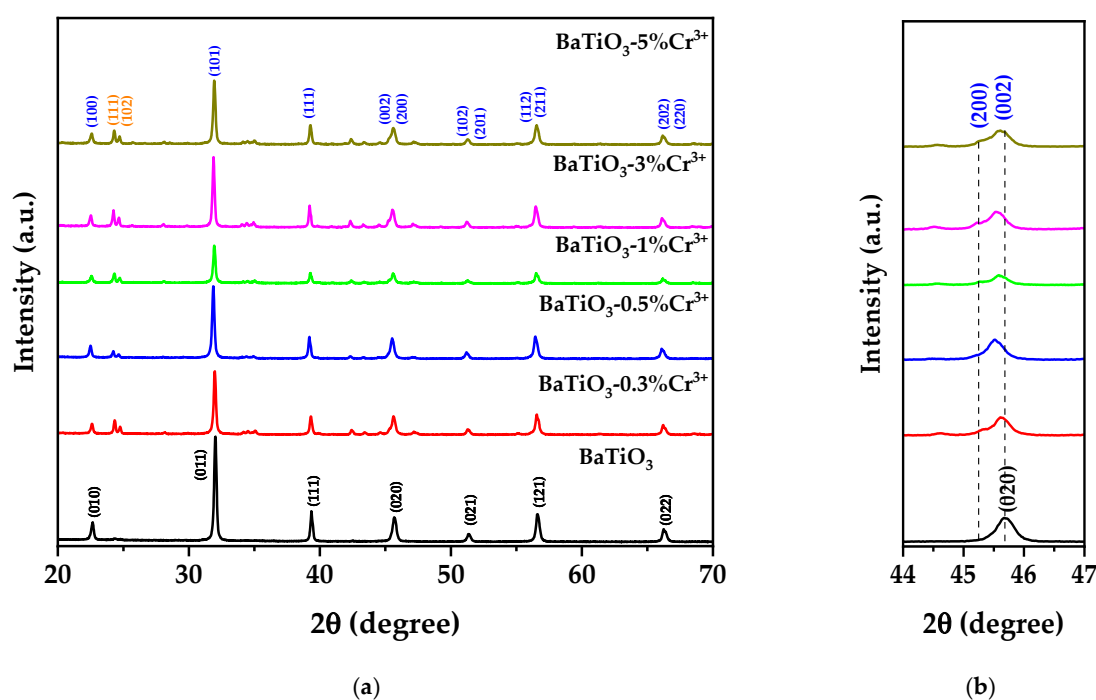


Figure 2. (a) X-ray diffraction patterns of pure and doped BaTiO_3 and (b) amplification of XRD peaks within the $44\text{--}46.5^\circ$ range.

The effectiveness of using chromium nitrate dissolved in 2-propanol for Cr^{3+} incorporation is demonstrated by the systematic evolution of the XRD patterns with increasing dopant concentration. The homogeneous distribution of Cr^{3+} ions achieved through the sol–gel route enables uniform substitution at the A-site, as evidenced by the consistent peak splitting patterns across different doping levels.

The minor peaks observed around 24.37° , 24.78° , 34.83° , 42.45° , 43.46° , and 46.9° can be attributed to trace amounts of BaCO_3 (COD: 96-900-6842), formed by the reaction of

Ba²⁺ with atmospheric CO₂ during synthesis. These peaks correspond to the (111), (102), (013), (203), (104), and (114) planes of BaCO₃, respectively.

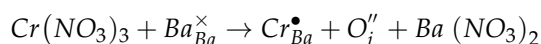
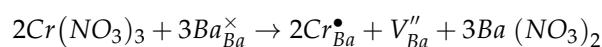
The sol–gel synthesis approach using chromium nitrate in 2-propanol plays a crucial role in achieving the observed structural characteristics, where molecular-level mixing in the sol state and controlled hydrolysis and condensation reactions enable precise control over the Cr³⁺ substitution process. This is particularly important given the significant difference in ionic radii between Ba²⁺ (1.35 Å) and Cr³⁺ (0.69 Å). Furthermore, the sol–gel method has demonstrated versatility in accommodating various dopants, such as calcium [39], lanthanum [40], and cerium [41], among others [17,42], which have smaller ionic radii compared to Ba²⁺.

The Rietveld refinement analysis (Figure S2) reveals systematic changes in structural parameters with increasing Cr³⁺ content, as presented in Table 1. The pristine BaTiO₃ sample exhibits equal lattice parameters ($a = b = c = 4.00785$ Å) and 90° angles between them, characteristic of the cubic phase. Upon Cr³⁺ doping, the structural transition to the tetragonal symmetry, with the $a = b$ lattice parameter decreasing from 4.00698 Å to 4.00379 Å, and the c parameter increasing from 4.01477 Å to 4.01699 Å (Figure S3) [43,44].

Table 1. Structural parameters of chromium-doped BaTiO₃ nanoparticles.

Structural Parameter	Sample					
	BaTiO ₃	BaTiO ₃ -0.3%Cr ³⁺	BaTiO ₃ -0.5%Cr ³⁺	BaTiO ₃ -1%Cr ³⁺	BaTiO ₃ -3%Cr ³⁺	BaTiO ₃ -5%Cr ³⁺
Crystal system	Cubic	Tetragonal	Tetragonal	Tetragonal	Tetragonal	Tetragonal
Space group	Pm-3m	P4mm	P4mm	P4mm	P4mm	P4mm
A = b (Å)	4.00785	4.00698	4.00554	4.00599	4.00476	4.00379
c (Å)	4.00785	4.01477	4.01602	4.01555	4.01558	4.01699
α = β = γ (°)	90	90	90	90	90	90
ρ(g/cm ³)	6.01	6.01	6.01	6	6.01	6.01
D (nm)	63.27	55.29	54.49	54.61	57.71	58.27
Micro strain (%)	0.097	0.063	0.056	0.062	0.053	0.046
R _{exp} (%)	2.25336	2.37418	2.386	3.25221	2.36559	2.34574
R _p (%)	2.82395	3.21306	4.25722	3.53244	3.24347	3.31153
R _{wp} (%)	4.08684	4.30687	6.03794	4.50786	4.29443	4.37974
GOF	1.81367	1.81405	2.53057	1.38609	1.81537	1.8671

The defect chemistry associated with this A-site substitution can be described using Kröger–Vink notation:



where Cr_{Ba}^{\bullet} represents Cr³⁺ on a Ba²⁺ site (single positive charge), V_{Ba}'' represents a barium vacancy (double negative charge), and O_i'' represents an oxygen interstitial (double negative charge).

The crystallite size analysis shows a marked decrease from 63.27 nm (pristine) to 55.29 nm (0.3% Cr³⁺), followed by relatively stable values around 54–58 nm for higher doping levels. The micro strain analysis from the Rietveld refinement shows values decreasing from 0.097% (pristine) to 0.046% (5% Cr³⁺), indicating that despite the significant size mismatch between Ba²⁺ and Cr³⁺, the sol–gel synthesis conditions enabled the formation of a relatively stable crystal structure [38].

3.3. Raman Spectroscopy

The Raman spectra (Figure 3) provide detailed insights into the local structural changes induced by A-site Cr³⁺ substitution in BaTiO₃. The pristine BaTiO₃ (Figure 3a) exhibits characteristic first-order vibrational modes with F_{2g} symmetry, representing symmetric

Ti-O bending (305 cm^{-1}) and stretching (720 cm^{-1}) motions. These modes reflect the cubic symmetry of the undoped structure, where TiO_6 octahedra maintain regular coordination geometry [45].

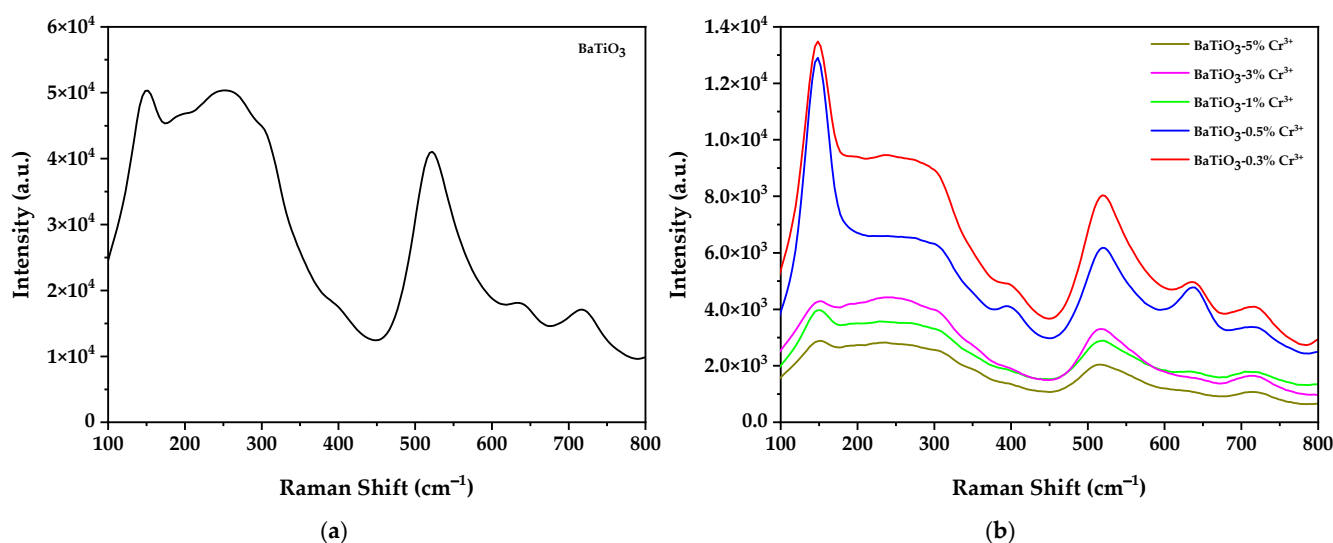


Figure 3. Raman spectra of (a) Pristine BaTiO_3 and (b) Cr^{3+} -doped BaTiO_3 .

Upon Cr^{3+} incorporation at the A-site (Figure 3b), systematic changes in the vibrational spectra emerge, reflecting the modified crystal structure. The development of additional modes at 153 , 521 , 637 , and 719 cm^{-1} indicates increasing lattice distortion with Cr^{3+} content. These spectral changes can be attributed to the formation of defect complexes ($\text{Cr}_{\text{Ba}'}^{\bullet}$, $\text{V}_{\text{Ba}'}''$, and O_i'') that modify local symmetry, strain fields created by the significant size mismatch between Cr^{3+} and Ba^{2+} , and enhanced displacement of Ti^{4+} ions from their central positions in response to the modified A-site environment [46].

The systematic evolution of peak intensities and the emergence of new vibrational features correlate with the increasing tetragonal distortion observed in XRD analysis. Notably, samples with higher Cr^{3+} content (1%, 3%, and 5%) show more pronounced spectral changes, consistent with greater structural modification at elevated doping levels. The low-frequency band at 153 cm^{-1} can be assigned to A-site cation motions, while the additional features in the $500\text{--}700\text{ cm}^{-1}$ range reflect modified Ti-O bonding environments resulting from the accommodation of Cr^{3+} in the lattice [18,21,47]. These spectroscopic observations provide compelling evidence for the successful incorporation of Cr^{3+} at the A-site and the consequent local structural modifications, despite the significant ionic radius mismatch. The Raman data thus support our proposed defect compensation mechanism and provides valuable insights into the local structural changes that enable stable A-site substitution in this system [48].

3.4. Fourier-Transform Infrared Spectroscopy (FTIR)

FTIR spectra (Figure 4) reveal systematic modifications in the vibrational characteristics of BaTiO_3 upon A-site Cr^{3+} substitution. The spectrum of pristine BaTiO_3 shows characteristic absorption bands at 507 cm^{-1} (Ti-O bending), 632 cm^{-1} (asymmetric O-Ti-O stretching), 857 cm^{-1} (asymmetric Ti-O-Ti bridging stretch), and 1417 cm^{-1} (Ti-O stretch), consistent with previous reports [49,50]. Upon Cr^{3+} incorporation, several systematic changes emerge in the spectral features. The relative intensity of the 507 cm^{-1} band decreases with increasing Cr^{3+} content, while new features develop in the $600\text{--}700\text{ cm}^{-1}$ region. These changes reflect modifications in the Ti-O bonding environments induced by the accommodation of Cr^{3+} at the A-site [51].

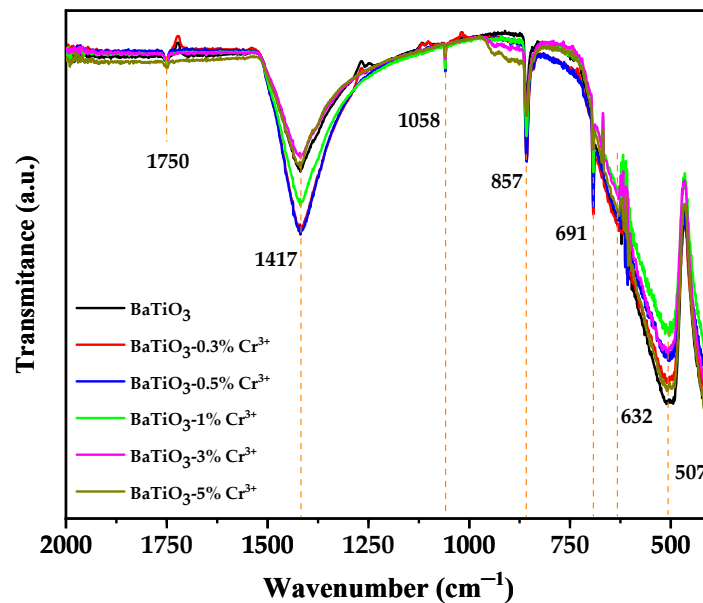


Figure 4. FTIR spectra of pure and Cr³⁺-doped BaTiO₃.

The band at 695 cm⁻¹, associated with symmetric O-Ti-O stretching in TiO₆ octahedra, shows progressive modification in intensity and shape with increasing Cr³⁺ concentration [48]. This evolution indicates that A-site substitution influences the local symmetry of the octahedral units, likely through the formation of defect complexes involving barium vacancies and oxygen interstitials. The high-frequency mode at 1417 cm⁻¹, corresponding to localized oxygen vibrations, exhibits systematic changes in intensity that correlate with the increasing Cr³⁺ content [52]. Additional weak features observed in samples with higher Cr³⁺ concentrations may indicate the presence of trace secondary phases, although these remain below the detection limit of XRD [53].

The systematic evolution of the FTIR spectra provides further evidence for the successful incorporation of Cr³⁺ at the A-site and the resulting modifications in the local bonding environments. The observed spectral changes align with our proposed defect compensation mechanism, where the significant size mismatch between Cr³⁺ and Ba²⁺ is accommodated through the formation of ordered defect structures. These spectroscopic signatures complement our XRD and Raman analyses, offering additional insights into the local structural modifications that enable stable A-site substitution in this system.

3.5. UV-Visible Spectroscopy

The UV-vis diffuse reflectance spectra, as shown in Figure 5a, reveal the influence of Cr³⁺ doping on the optical properties of BaTiO₃. Pure BaTiO₃ exhibits a sharp absorption edge and low reflectance below 375 nm, indicating its wide bandgap and strong UV absorption. As the Cr³⁺ doping concentration increases, the reflectance progressively decreases across the visible range, correlating with a visible color change from white for undoped BaTiO₃ to pale grey hues in the doped ceramics. This qualitative observation suggests a narrowing of the bandgap due to Cr³⁺ incorporation.

To quantitatively evaluate the optical bandgap values, the Kubelka–Munk function, which relates the absorption coefficient to diffuse reflectance, was employed. The Kubelka–Munk function, $F(R)$, is defined as:

$$F(R) = \frac{K}{S} = \frac{(1 - R)^2}{2R}$$

where K is the absorption coefficient of radiation, S is the scattering factor, and R is the ratio of the intensities of radiation reflected in a diffuse manner. This function assumes

that the transitions occur between extended states, consistent with the electronic structure of BaTiO₃.

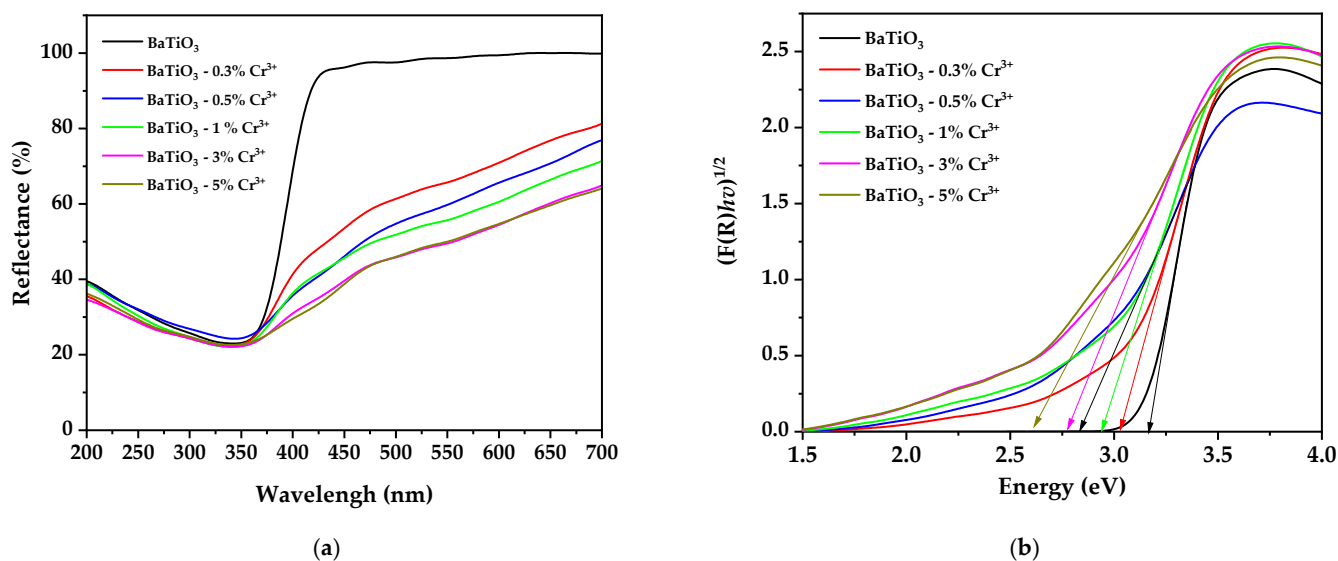


Figure 5. (a) UV-visible diffuse reflectance spectrum. (b) Kubelka–Munk plot for bandgap calculation.

The calculated bandgap values demonstrate a monotonic decline from 3.168 eV for pure BaTiO₃ to 3.03 eV (0.3% Cr³⁺), 2.939 eV (0.5% Cr³⁺), 2.834 eV (1% Cr³⁺), 2.775 eV (3% Cr³⁺), and finally to 2.604 eV in the 5% Cr³⁺-substituted composition, validating the significant bandgap engineering achieved through controlled Cr³⁺ dopant inclusion.

The slightly enhanced bandgap reduction observed at 1% Cr³⁺ doping suggests an optimal configuration of defect complexes at this concentration, leading to more effective modification of the electronic band structure.

This quantifies the magnitude of bandgap engineering achieved through controlled dopant inclusion. The decrease in bandgap energy with increasing Cr³⁺ concentration can be attributed to the increased hybridization between the Cr 3*d* and O 2*p* orbitals localized within the distorted TiO₆ octahedral units [54,55]. The structural transitions induced by Cr³⁺ doping, as evidenced by XRD and Raman spectroscopy, enhance the bonding covalence, facilitating the reduction in bandgap energy.

Moreover, the polarization-strain effects associated with the tetragonal distortion in Cr³⁺-doped BaTiO₃ can assist in charge carrier separation and mobility, further contributing to the observed optical properties. The introduction of Cr³⁺ dopants also creates mid-gap states, which can act as intermediate energy levels for sub-bandgap optical absorption [56]. These mid-gap states allow for the absorption of photons with energies lower than the intrinsic bandgap of BaTiO₃, effectively extending the absorption range into the visible region.

3.6. Photoluminescence Spectroscopy

The photoluminescence (PL) spectra of pure and Cr³⁺-doped BaTiO₃ samples (Figure 6), recorded under carefully controlled experimental conditions (excitation: 254 nm, temperature: 25 °C, and fixed illumination area), reveal complex emission behavior reflecting the electronic structure modifications induced by A-site substitution. Gaussian deconvolution analysis (Figure S4, $R^2 > 0.999$) demonstrates the presence of multiple emission components, indicating diverse radiative recombination pathways in the material.

The pristine BaTiO₃ exhibits three primary emission components centered at 361.17, 396.74, and 415.92 nm, with relative contributions of 7.08%, 41.17%, and 51.75%, respectively (Table S1). The dominant peak at 415.92 nm (FWHM = 47.69 nm) originates from radiative recombination involving oxygen vacancy states, while the bands at 361.17 nm (FWHM = 60.64 nm) and 396.74 nm (FWHM = 32.77 nm) correspond to near-band-edge

transitions and shallow defect states [57], respectively. Upon Cr^{3+} incorporation, the emergence of a fourth emission component ($\sim 430\text{--}433\text{ nm}$) is observed in all doped samples, with systematically varying intensity and FWHM values. This new emission band can be attributed to electronic transitions involving the Cr^{3+} -induced defect complexes ($\text{Cr}_{\text{Ba}}^{\bullet}$, V_{Ba}'' and O_i'') [58].

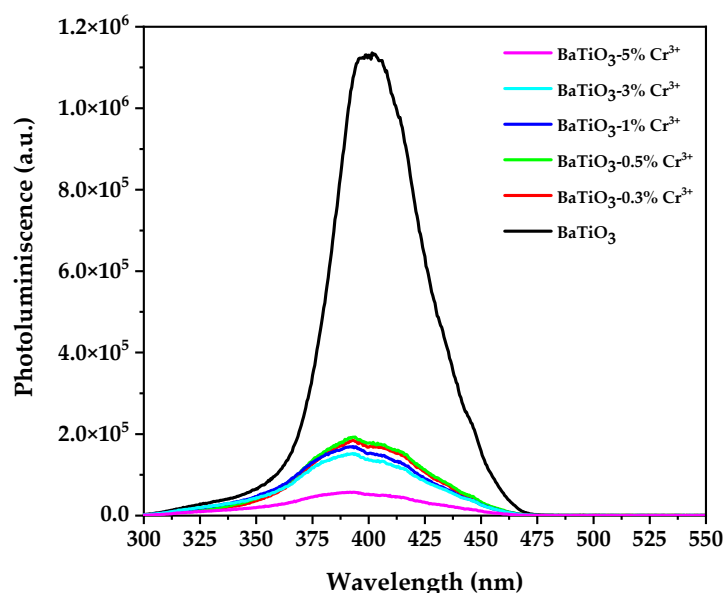


Figure 6. Photoluminescence spectra of pure and Cr^{3+} -doped BaTiO_3 .

A notable feature is the progressive decrease in overall PL intensity with increasing Cr^{3+} concentration, particularly pronounced for 3%- and 5%-doped samples, where the integrated intensity decreases to approximately 45% and 25% of the pristine value, respectively. This reduction correlates with the enhanced tetragonal distortion and increased defect concentration, suggesting that a higher Cr^{3+} content promotes non-radiative recombination pathways [59]. The relative contributions of emission components also evolve systematically, with the second peak (392–396 nm) maintaining a dominant contribution ($\sim 68\text{--}72\%$) in doped samples while the intensity of the third peak decreases significantly. Peak positions show subtle but consistent shifts ($\Delta\lambda \leq 3\text{ nm}$) with increasing Cr^{3+} content, indicating modification of the local electronic environment around emission centers.

The evolution of PL characteristics provides valuable insights into the defect structure and electronic properties of Cr^{3+} -doped BaTiO_3 . The appearance of the fourth emission component and the modification of existing emission intensities directly reflect the formation and interaction of defect complexes arising from A-site Cr^{3+} substitution [60]. These spectroscopic signatures, combined with the observed trends in peak parameters and overall intensity, strongly support our proposed model of defect-mediated accommodation of Cr^{3+} at the Ba^{2+} site. The high quality of peak deconvolution ($R^2 > 0.999$) and the systematic nature of spectral changes across the doping series provide robust evidence for the proposed electronic structure modifications.

3.7. Transmission Electron Microscopy

The transmission electron microscopy (TEM) analysis elucidates the morphological and structural evolution of Cr^{3+} -doped BaTiO_3 nanoparticles as a function of dopant concentration (Figure 7). Quantitative size distribution analysis, based on measurements of over 100 particles per sample with uniform 10 nm interval widths (Figure S3a–f), reveals systematic changes in particle size statistics. The pristine BaTiO_3 exhibits a broad size distribution with mean diameter $74.52 \pm 74.04\text{ nm}$ and median 48.59 nm, indicating significant size polydispersity. Upon Cr^{3+} incorporation, a dramatic reduction in both average size and distribution width is observed, with the 0.3% Cr^{3+} -doped sample showing a narrower

distribution with mean 33.46 ± 28.82 nm and median 32.954 nm, suggesting more uniform nucleation and growth dynamics. Further doping reveals systematic evolution in particle statistics, with 0.5% Cr^{3+} showing a mean of 32.84 ± 19.29 nm (median 27.98 nm), 1.0% Cr^{3+} with a mean of 33.61 ± 17.44 nm (median 26.77 nm), 3.0% Cr^{3+} displaying a mean of 40.02 ± 25.30 nm (median 32.94 nm), and 5.0% Cr^{3+} exhibiting means of 42.71 ± 24.18 nm (median 35.89 nm). The size distributions follow a lognormal pattern, with decreasing skewness at higher doping concentrations, suggesting more controlled particle growth [15].

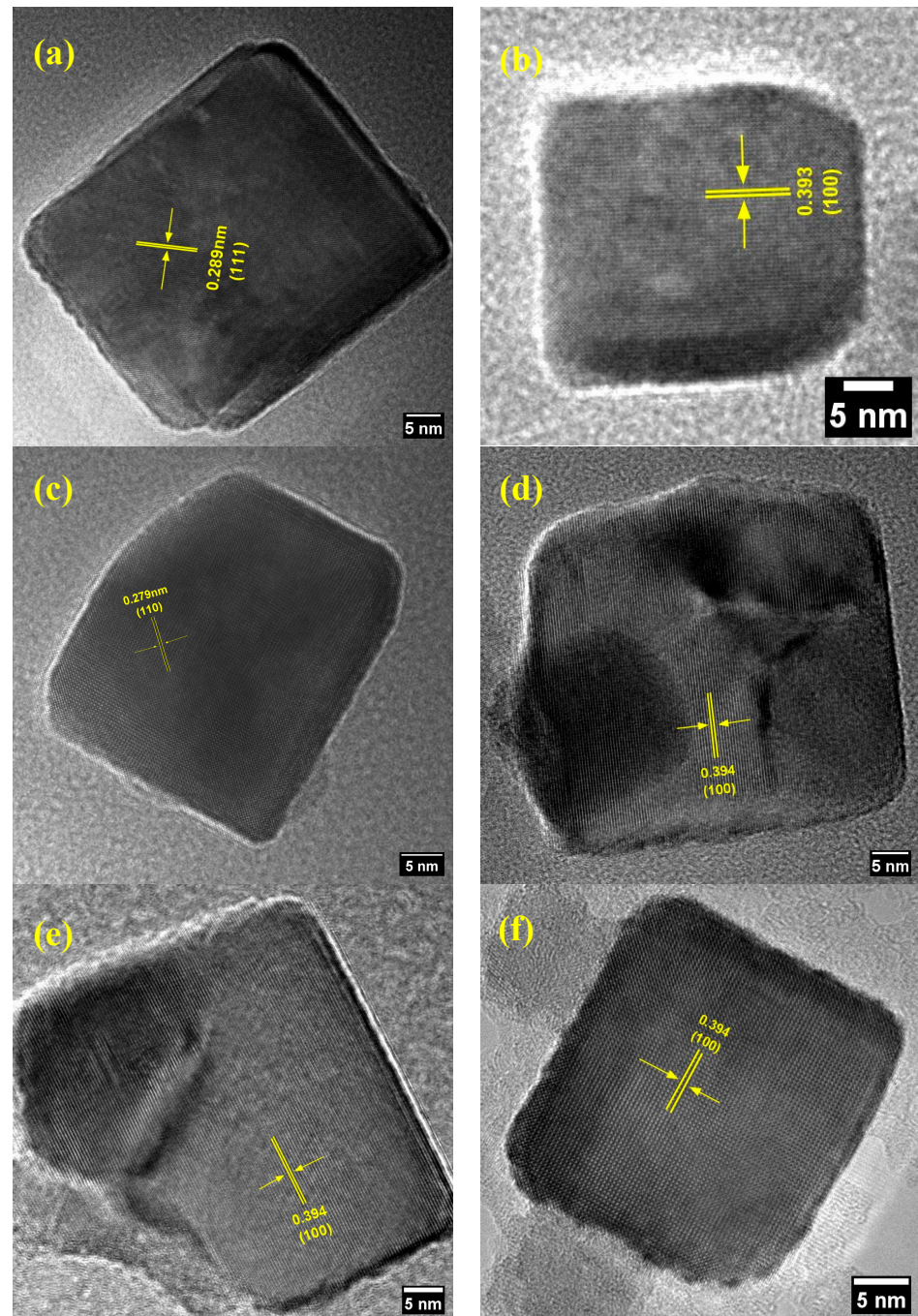


Figure 7. Transmission electron microscopy microphotography of (a) BaTiO₃, (b) BaTiO₃-0.3%Cr³⁺, (c) BaTiO₃-0.5%Cr³⁺, (d) BaTiO₃-1%Cr³⁺, (e) BaTiO₃-3%Cr³⁺, and (f) BaTiO₃-5%Cr³⁺.

High-resolution TEM (HRTEM) analysis reveals well-resolved lattice fringes, enabling direct measurement of interplanar spacings. The pristine BaTiO₃ (Figure 7a) shows clear

lattice fringes with a d-spacing of 0.289 nm, corresponding to the (111) planes. Upon Cr³⁺ doping, systematic variations in the lattice parameters are observed. The 0.3% Cr³⁺-doped sample (Figure 7b) exhibits lattice fringes with d = 0.393 nm indexed to (100) planes, while the 0.5% Cr³⁺-doped sample (Figure 7c) shows fringes with d = 0.279 nm corresponding to (110) planes. The 1%, 3%, and 5% Cr³⁺-doped samples (Figure 7d–f) display interplanar spacings of 0.394 nm, all corresponding to (100) planes.

Energy-dispersive X-ray spectroscopy (EDX) analysis (Table 2) quantitatively confirms the successful and controlled incorporation of Cr³⁺, with atomic concentrations incrementing from 0.46 atom% for 0.3% nominal Cr³⁺-doping to 1.64 atom% for 5% nominal Cr³⁺-doping. The remarkable reduction in particle size upon initial Cr³⁺ doping (0.3–1.0%) suggests that even small amounts of dopant significantly alter the nucleation dynamics. The subsequent gradual increase in particle size at higher doping levels (3–5% Cr³⁺) indicates a transition in the growth mechanism, possibly due to the increased concentration of defect complexes affecting crystal growth kinetics [61].

Table 2. Energy dispersive X-ray spectroscopy (EDX) analysis of all samples.

Element	Sample					
	BaTiO ₃	BaTiO ₃ - 0.3%Cr ³⁺	BaTiO ₃ - 0.5%Cr ³⁺	BaTiO ₃ - 1%Cr ³⁺	BaTiO ₃ - 3%Cr ³⁺	BaTiO ₃ - 5%Cr ³⁺
Ba (Atom %)	18.06	14.81	16.35	16.91	17.62	13.34
Ti (Atom %)	18.13	15.39	17.67	17.57	18.87	14.92
O (Atom %)	58.53	52.66	51.17	50.16	47.08	53.61
Cr (Atom %)	-	0.46	0.57	0.97	1.32	1.64
C (Atom%)	5.28	16.68	14.24	14.39	15.11	16.49
Total (%)	100	100	100	100	100	100

The convergence of mean and median values with increasing Cr³⁺ content indicates enhanced size uniformity, particularly evident in the 3% and 5% doped samples, suggesting a more controlled growth process mediated by the presence of dopant-induced defect complexes [15].

3.8. DPPH Radical Antioxidant Activity

The antioxidant activity of pure and Cr³⁺-doped BaTiO₃ nanoparticles was evaluated using the DPPH assay, which measures the ability of the nanoparticles to scavenge stable free radicals. Figure 8 shows that the scavenging percentages obtained from the assay provide valuable insights into the radical scavenging potential of the nanoparticles at different concentrations (125, 250, 500, and 1000 µg/mL). Pure BaTiO₃ nanoparticles exhibited relatively stable scavenging percentages across the tested concentrations, ranging from 40.70% to 43.33%, indicating their inherent antioxidant properties. On the other hand, Cr³⁺-doped BaTiO₃ nanoparticles displayed a more pronounced variation in scavenging percentages, particularly at higher concentrations. At lower concentrations (125 and 250 µg/mL), the Cr³⁺-doped samples showed scavenging percentages comparable to or slightly lower than pure BaTiO₃. However, as the concentration increased to 500 and 1000 µg/mL, the scavenging percentages of Cr³⁺-doped samples tended to decrease, especially for higher doping concentrations (3% and 5% Cr³⁺). This trend suggests that the incorporation of Cr³⁺ into the BaTiO₃ lattice influences the antioxidant activity of the nanoparticles, likely due to structural modifications, electronic effects, and changes in surface chemistry. The structural transition from cubic to tetragonal phase induced by Cr³⁺ doping may affect the surface properties and reactivity of the nanoparticles [49], impacting their ability to interact with and neutralize DPPH radicals [62]. Additionally, the alteration of the electronic structure and band gap of the material, as well as the presence of Cr³⁺ ions on the surface, may influence the electron transfer processes involved in the scavenging of DPPH radicals [63], leading to a decrease in antioxidant activity at higher doping concentrations.

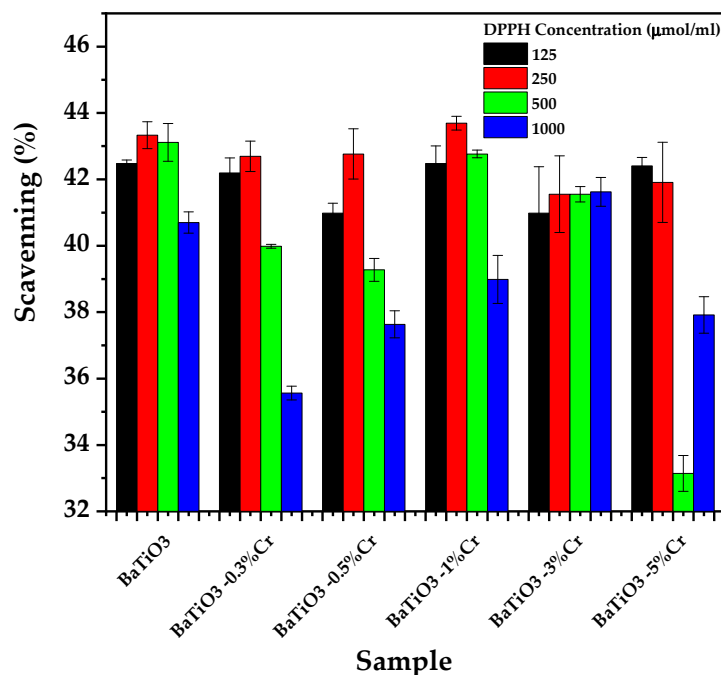


Figure 8. Antioxidant activity of pure and Cr³⁺-doped BaTiO₃.

A comprehensive analysis of the antioxidant activity of Cr³⁺-doped BaTiO₃ nanoparticles was conducted using a two-way analysis of variance (ANOVA) (Table 3). The results revealed highly significant main effects for both the sample type ($F(5, 48) = 47.45, p < 0.001$) and DPPH concentration ($F(3, 48) = 58.70, p < 0.001$). Furthermore, a strong interaction effect between sample type and DPPH concentration was observed ($F(15, 48) = 23.99, p < 0.001$). These findings provide robust evidence that the level of Cr³⁺ doping in BaTiO₃ nanoparticles significantly influences their antioxidant activity, and this effect is markedly dependent on the DPPH concentration used in the assay. The substantial interaction effect underscores a complex relationship between Cr³⁺ doping and DPPH concentration, highlighting the critical importance of considering both factors when evaluating the antioxidant properties of these nanoparticles. The use of triplicate measurements enhances the reliability of these results.

Table 3. ANOVA results.

Source of Variation	Degrees of Freedom	Sum of Squares	Mean Square	F-Value	p-Value
Sample	5	362.76	72.552	47.45	<0.001
Concentration	3	269.28	89.76	58.7	<0.001
Sample × Concentration	15	550.23	36.682	23.99	<0.001
Residuals	48	73.41	1.529		

3.9. Antibacterial Activity

The antibacterial activity of pure and Cr³⁺-doped BaTiO₃ nanoparticles against *E. coli*, evaluated using the Kirby–Bauer disk diffusion method (Figure S4), reveals a complex relationship between the Cr³⁺ doping concentration and antibacterial efficacy (Table 4). Deionized water, used as a negative control, showed no inhibition zone, confirming the specificity of the observed antibacterial effects to the nanoparticle treatments. Pure BaTiO₃ nanoparticles exhibited stable inhibition zone diameters (8.988–9.886 mm) across the tested concentrations (0.5–4 mg/mL), indicating inherent antibacterial properties attributed to reactive oxygen species (ROS) generation and bacterial membrane disruption [64]. Cr³⁺ doping significantly influenced this activity, with a non-linear trend observed. At low Cr³⁺ concentrations (0.3% and 0.5%), antibacterial activity was enhanced, particularly at higher

nanoparticle concentrations (1.5–4 mg/mL), with the 0.5% Cr³⁺-doped sample showing peak performance (10.569 mm at 1.5 mg/mL). This enhancement likely stems from optimal structural distortion, as evidenced by XRD results showing the cubic-to-tetragonal transition, combined with the introduction of non-radiative recombination centers observed in the PL spectra, which may facilitate enhanced ROS generation and bacterial interaction [65]. However, at higher Cr³⁺ concentrations (1%, 3%, and 5%), the antibacterial efficacy decreased, with 5% Cr³⁺-doping exhibiting the lowest activity (6.892–8.992 mm). This decline can be attributed to several factors: excessive structural distortion, as indicated by XRD and Raman spectroscopy, potentially affecting surface reactivity and bacterial membrane interaction; electronic structure modifications, revealed by PL and UV-vis spectroscopy, possibly leading to less efficient ROS generation; and surface property changes, evidenced by the broadening of PL emission peaks and TEM observations of increased surface roughness, potentially reducing active sites for bacterial interaction. The incorporation of Cr³⁺ ions into the BaTiO₃ lattice alters the electronic structure and band gap of the material [38,66], influencing the generation and transfer of ROS, which play a crucial role in the antibacterial mechanism of metal oxide nanoparticles. At higher Cr³⁺ doping concentrations, these electronic modifications may become less favorable for efficient ROS generation and transfer, thereby reducing antibacterial efficacy. Additionally, the presence of Cr³⁺ ions on the nanoparticle surface may modify surface chemistry and the availability of reactive sites for bacterial cell interaction, potentially leading to a saturation of surface sites at higher doping levels and reducing overall antibacterial efficiency. The observed trends align with the complex interplay between structural transitions, electronic structure modifications, and surface property changes induced by Cr³⁺ doping. The optimal 0.5% Cr³⁺ concentration likely represents a balance point where these factors synergistically enhance antibacterial activity, while higher concentrations lead to detrimental effects.

Table 4. Inhibition zones at various concentrations of pure and doped BaTiO₃.

Concentration (mg/mL)	Zone of Inhibition (mm)									
	0.5	SD	1	SD	1.5	SD	2	SD	4	SD
BaTiO ₃	9.602	0.318	9.886	0.323	9.707	0.273	8.988	0.328	9.407	0.122
BaTiO ₃ -0.3%Cr ³⁺	9.506	0.092	8.181	0.119	8.319	0.143	8.893	0.293	9.899	0.309
BaTiO ₃ -0.5%Cr ³⁺	9.525	0.348	9.815	0.145	10.569	0.194	9.309	0.344	10.510	0.219
BaTiO ₃ -1%Cr ³⁺	8.296	0.137	8.267	0.131	8.864	0.298	9.721	0.079	8.384	0.267
BaTiO ₃ -3%Cr ³⁺	8.870	0.307	8.745	0.147	9.123	0.299	9.582	0.101	8.940	0.073
BaTiO ₃ -5%Cr ³⁺	6.892	0.127	7.250	0.148	7.802	0.238	8.404	0.143	8.992	0.185

4. Conclusions

This comprehensive study on Cr³⁺-doped BaTiO₃ nanoparticles demonstrates that controlled Cr³⁺ doping induces significant modifications across multiple material properties. The sol-gel synthesis yields well-crystallized nanoparticles with a systematic size evolution, showing an initial decrease from 74.52 nm to 33.46 nm at 0.3% Cr³⁺ followed by a gradual increase to 42.71 nm at 5% Cr³⁺. Structural characterization reveals a cubic-to-tetragonal phase transition upon doping, accompanied by systematic changes in lattice parameters and the formation of defect complexes. The optical properties show remarkable tunability, with bandgap reduction from 3.168 eV to 2.604 eV and systematic modifications in photoluminescence characteristics, including the emergence of new emission components and controlled intensity variations. Vibrational spectroscopy confirms the structural transitions through systematic changes in Raman and FTIR modes. High-resolution TEM analysis reveals systematic variations in lattice spacings and morphology, while EDX confirms successful dopant incorporation up to 1.64 atom%. The bioactive properties exhibit concentration-dependent behavior, with optimal antibacterial activity at 0.5% Cr³⁺ doping (10.569 mm inhibition zone) and sustained antioxidant activity in pure and Cr³⁺-doped BaTiO₃. These findings establish clear structure-property relationships in Cr³⁺-doped

BaTiO₃ nanoparticles and demonstrate their potential for applications ranging from electronics to biomedicine. Future research directions should include investigations into long-term stability, exploration of co-doping strategies, and in-depth mechanistic studies to further optimize these multifunctional nanomaterials for next-generation applications.

Supplementary Materials: The following supporting information can be downloaded at: <https://www.mdpi.com/article/10.3390/cryst14110998/s1>, Figure S1: COD X-ray diffraction standard; Figure S2: Rietveld refinement plots; Figure S3: Influence of dopant concentration on BaTiO₃ lattice constant and the tetragonality; Figure S4: Deconvolution peaks; Figure S5: TEM particle size distribution and micrographs; Figure S6: Inhibition zone; Table S1: Deconvolution parameters.

Author Contributions: Conceptualization, E.M.F. and J.A.C.G.; methodology J.C.H.H., E.J.S.S., E.M.F. and J.A.C.G.; software, E.J.S.S.; validation, C.A.P.B. and H.E.N.M.; formal analysis, J.C.H.H. and H.E.N.M.; investigation, J.C.H.H., R.M.T.C., B.S.V.B. and G.d.L.F.Q.; resources, F.G.G. and A.B.Q.C.; data curation, J.C.H.H., G.d.L.F.Q. and C.A.P.B.; writing—original draft preparation, J.C.H.H., B.S.V.B. and E.J.S.S.; writing—review and editing, E.M.F., B.S.V.B., A.B.Q.C. and E.J.S.S.; visualization, J.C.H.H., G.d.L.F.Q. and E.J.S.S.; supervision, C.A.P.B. and E.M.F.; project administration, E.M.F. and J.A.C.G.; funding acquisition, E.M.F., J.A.C.G. and B.S.V.B. All authors have read and agreed to the published version of the manuscript.

Funding: This research was funded by the Universidad Nacional Jorge Basadre Grohmann through “Fondos del canon sobrecanon y regalías mineras”, with the projects “Estudio de materiales ferroeléctricos (BiFeO₃ y Bi₂FeCrO₆)” and “Determinación de huellas digitales ópticas, de materiales sólidos, líquidos y orgánicos mediante espectroscopia visible e infrarroja” approved with the resolutions N° 5854-2019-UN/JBG and N° 4516-2018-UN/JBG, respectively. The project “Caracterización microestructural de un antibiótico boratado, obtenido de boro residual, y su aplicación en el diseño de recubrimientos fotocatalíticos urbanos antibacterianos” was approved through resolution R.C.O N° 352-2022-UNAM.

Data Availability Statement: The author confirms that all obtained during this study are included in this published article and its supplementary material.

Acknowledgments: We are grateful to Universidad Nacional Jorge Basadre Grohman and the projects, “Estudio de materiales ferroeléctricos (BiFeO₃ y Bi₂FeCrO₆) y su aplicación en celdas solares”, “Determinación de huellas digitales ópticas, de materiales sólidos, líquidos y orgánicos mediante espectroscopia visible e infrarroja”, and “Generación fotocatalítica y foto-electrocatalítica de hidrógeno en la región Tacna empleando nanopartículas de NiTiO₃ puras y dopadas”, approved by rectoral resolutions N° 4516-2018-UN/JBG, N° 5854-2019-UN/JBG, and N° 9155-2021-UN/JBG, respectively, for their support. The author Bertha Silvana Vera Barrios expresses her gratitude to the National University of Moquegua and to her project “Caracterización microestructural de un antibiótico boratado, obtenido de boro residual, y su aplicación en el diseño de recubrimientos fotocatalíticos urbanos antibacterianos”, which was approved through resolution R.C.O N° 352-2022-UNAM. The author Elisban Juani Sacari Sacari gratefully acknowledges the financial support provided by CONCYTEC through the PROCENCIA program under the “Becas en programas de doctorado en alianzas interinstitucionales” competition, according to contracts N°PE501088673-2024-PROCENCIA-BM and N°PE501084296-2023-PROCENCIA-BM for undertaking a Doctoral program in Physics at the Universidad Nacional de Ingeniería, Peru.

Conflicts of Interest: The authors declare no conflicts of interest.

References

1. Jain, A.; Kumar, A.; Gupta, N.; Kumar, K. Advancements and challenges in BaTiO₃-Based materials for enhanced energy storage. *Mater. Today Proc.* 2024, *in press*. [[CrossRef](#)]
2. Masekela, D.; Hintsho-Mbita, N.C.; Sam, S.; Yusuf, T.L.; Mabuba, N. Application of BaTiO₃-based catalysts for piezocatalytic, photocatalytic and piezo-photocatalytic degradation of organic pollutants and bacterial disinfection in wastewater: A comprehensive review. *Arab. J. Chem.* 2023, *16*, 104473. [[CrossRef](#)]
3. Sood, A.; Desseigne, M.; Dev, A.; Maurizi, L.; Kumar, A.; Millot, N.; Han, S.S. A Comprehensive Review on Barium Titanate Nanoparticles as a Persuasive Piezoelectric Material for Biomedical Applications: Prospects and Challenges. *Small* 2023, *19*, e2206401. [[CrossRef](#)] [[PubMed](#)]

4. Lang, X.Y.; Jiang, Q. Size and interface effects on Curie temperature of perovskite ferroelectric nanosolids. *J. Nanopart. Res.* **2007**, *9*, 595–603. [[CrossRef](#)]
5. Jiang, Q.; Cui, X.F.; Zhao, M. Size effects on Curie temperature of ferroelectric particles. *Appl. Phys. A Mater. Sci. Process.* **2004**, *78*, 703–704. [[CrossRef](#)]
6. Wada, S.; Hoshina, T.; Yasuno, H.; Ohishi, M.; Kakemoto, H.; Tsurumi, T.; Yashima, M. Size Effect of Dielectric Properties for Barium Titanate Particles and Its Model. *Key Eng. Mater.* **2006**, *301*, 27–30. [[CrossRef](#)]
7. Shen, Z.-Y.; Li, J.-F. Enhancement of piezoelectric constant d_{33} in BaTiO₃ ceramics due to nano-domain structure. *J. Ceram. Soc. Jpn.* **2010**, *118*, 940–943. [[CrossRef](#)]
8. Lu, W.; Quilitz, M.; Schmidt, H. Nanoscaled BaTiO₃ powders with a large surface area synthesized by precipitation from aqueous solutions: Preparation, characterization and sintering. *J. Eur. Ceram. Soc.* **2007**, *27*, 3149–3159. [[CrossRef](#)]
9. Ashiri, R. On the solid-state formation of BaTiO₃ nanocrystals from mechanically activated BaCO₃ and TiO₂ powders: Innovative mechanochemical processing, the mechanism involved, and phase and nanostructure evolutions. *RSC Adv.* **2016**, *6*, 17138–17150. [[CrossRef](#)]
10. Suherman, B.; Nurosyid, F.; Khairuddin; Sandi, D.K.; Irian, Y. Impacts of low sintering temperature on microstructure, atomic bonds, and dielectric constant of barium titanate (BaTiO₃) prepared by co-precipitation technique. *J. Phys. Conf. Ser.* **2022**, *2190*, 12006. [[CrossRef](#)]
11. Hayashi, H.; Hakuta, Y. Hydrothermal Synthesis of Metal Oxide Nanoparticles in Supercritical Water. *Materials* **2010**, *3*, 3794–3817. [[CrossRef](#)] [[PubMed](#)]
12. Khort, A.A.; Podbolotov, K.B. Preparation of BaTiO₃ nanopowders by the solution combustion method. *Ceram. Int.* **2016**, *42*, 15343–15348. [[CrossRef](#)]
13. Choi, G.J.; Kim, H.S.; Cho, Y.S. BaTiO₃ particles prepared by microwave-assisted hydrothermal reaction using titanium acylate precursors. *Mater. Lett.* **1999**, *41*, 122–127. [[CrossRef](#)]
14. Kaviani, R.; Saidi, A. Sol-gel derived BaTiO₃ nanopowders. *J. Alloys Compd.* **2009**, *468*, 528–532. [[CrossRef](#)]
15. Navas, D.; Fuentes, S.; Castro-Alvarez, A.; Chavez-Angel, E. Review on Sol-Gel Synthesis of Perovskite and Oxide Nanomaterials. *Gels* **2021**, *7*, 275. [[CrossRef](#)]
16. Borlaf, M.; Moreno, R. Colloidal sol-gel: A powerful low-temperature aqueous synthesis route of nanosized powders and suspensions. *Open Ceram.* **2021**, *8*, 100200. [[CrossRef](#)]
17. Rahman, M.A. Understanding of doping sites and versatile applications of heteroatom modified BaTiO₃ ceramic. *J. Asian Ceram. Soc.* **2023**, *11*, 215–224. [[CrossRef](#)]
18. Issam, D.; Achehboune, M.; Boukhoubza, I.; Hatel, R.; El Adnani, Z.; Rezzouk, A. Investigation of the crystal structure, electronic and optical properties of Cr-doped BaTiO₃ on the Ti site using first principles calculations. *J. Phys. Chem. Solids* **2023**, *175*, 111209. [[CrossRef](#)]
19. Derkaoui, I.; Achehboune, M.; Boukhoubza, I.; El Adnani, Z.; Rezzouk, A. Improved first-principles electronic band structure for cubic (Pm 3⁻ m) and tetragonal (P4mm, P4/mmm) phases of BaTiO₃ using the Hubbard U correction. *Comput. Mater. Sci.* **2023**, *217*, 111913. [[CrossRef](#)]
20. Buscaglia, V.; Buscaglia, M.T.; Canu, G. *BaTiO₃-Based Ceramics: Fundamentals, Properties and Applications*. *Encyclopedia of Materials: Technical Ceramics and Glasses*; Elsevier: Amsterdam, The Netherlands, 2021; pp. 311–344. ISBN 9780128222331.
21. Amaechi, I.C.; Kolhatkar, G.; Youssef, A.H.; Rawach, D.; Sun, S.; Ruediger, A. B-site modified photoferroic Cr³⁺-doped barium titanate nanoparticles: Microwave-assisted hydrothermal synthesis, photocatalytic and electrochemical properties. *RSC Adv.* **2019**, *9*, 20806–20817. [[CrossRef](#)]
22. Ramakanth, S.; James Raju, K.C. Band gap narrowing in BaTiO₃ nanoparticles facilitated by multiple mechanisms. *J. Appl. Phys.* **2014**, *115*, 173507. [[CrossRef](#)]
23. Srilakshmi, C.; Saraf, R.; Prashanth, V.; Rao, G.M.; Shivakumara, C. Structure and Catalytic Activity of Cr-Doped BaTiO₃ Nanocatalysts Synthesized by Conventional Oxalate and Microwave Assisted Hydrothermal Methods. *Inorg. Chem.* **2016**, *55*, 4795–4805. [[CrossRef](#)] [[PubMed](#)]
24. Tewatia, K.; Sharma, A.; Sharma, M.; Kumar, A. Factors affecting morphological and electrical properties of Barium Titanate: A brief review. *Mater. Today Proc.* **2021**, *44*, 4548–4556. [[CrossRef](#)]
25. Ray, S.K.; Cho, J.; Hur, J. A critical review on strategies for improving efficiency of BaTiO₃-based photocatalysts for wastewater treatment. *J. Environ. Manag.* **2021**, *290*, 112679. [[CrossRef](#)] [[PubMed](#)]
26. Kumar, A.; Gori, Y.; Kumar, A.; Meena, C.S.; Dutt, N. (Eds.) *Advanced Materials for Biomedical Applications*, 1st ed.; Taylor and Francis: Boca Raton, FL, USA, 2023; ISBN 9781032356068.
27. Lay, R.; Deijs, G.S.; Malmström, J. The intrinsic piezoelectric properties of materials—A review with a focus on biological materials. *RSC Adv.* **2021**, *11*, 30657–30673. [[CrossRef](#)]
28. Tiburcio, J.; Sacari, E.; Chacaltana, J.; Medina, J.; Gamarra, F.; Polo, C.; Mamani, E.; Quispe, A. Influence of Cr Doping on Structural, Optical, and Photovoltaic Properties of BiFeO₃ Synthesized by Sol-Gel Method. *Energies* **2023**, *16*, 786. [[CrossRef](#)]
29. Anjos, P.d.; Pereira, E.C.; Gobato, Y.G. Study of the structure and optical properties of rare-earth-doped aluminate particles prepared by an amorphous citrate sol-gel process. *J. Alloys Compd.* **2005**, *391*, 277–283. [[CrossRef](#)]
30. Kao, C.-F.; Yang, W.-D. Preparation of barium strontium titanate powder from citrate precursor. *Appl. Organometal. Chem.* **1999**, *13*, 383–397. [[CrossRef](#)]

31. Pérez-Maqueda, L.A.; Diáñez, M.J.; Gotor, F.J.; Sayagués, M.J.; Real, C.; Criado, J.M. Synthesis of needle-like BaTiO₃ particles from the thermal decomposition of a citrate precursor under sample controlled reaction temperature conditions. *J. Mater. Chem.* **2003**, *13*, 2234–2241. [[CrossRef](#)]
32. Benyoussef, M.; Mura, T.; Saitzek, S.; Azrour, F.; Blach, J.-F.; Lahmar, A.; Gagou, Y.; El Marssi, M.; Sayede, A.; Jouiad, M. Nanostructured BaTi_{1-x}Sn_xO₃ ferroelectric materials for electrocaloric applications and energy performance. *Curr. Appl. Phys.* **2022**, *38*, 59–66. [[CrossRef](#)]
33. Sugawara, K.; Sakusabe, H.; Nishino, T.; Sugawara, T.; Ogiwara, K.; Dranoff, J.S. Thermal decomposition of barium titanate precursor prepared by a wet chemical method. *AIChE J.* **1997**, *43*, 2837–2843. [[CrossRef](#)]
34. Elmehdi, H.M.; Ramachandran, K.; Chidambaram, S.; Mani, G.T.; Pandiaraj, S.; Alqarni, S.A.; Daoudi, K.; Gaidi, M. Diode characteristics, piezo-photocatalytic antibiotic degradation and hydrogen production of Ce³⁺ doped ZnO nanostructures. *Chemosphere* **2024**, *350*, 141015. [[CrossRef](#)] [[PubMed](#)]
35. Qiao, L.; Bi, X. Microstructure and grain size dependence of ferroelectric properties of BaTiO₃ thin films on LaNiO₃ buffered Si. *J. Eur. Ceram. Soc.* **2009**, *29*, 1995–2001. [[CrossRef](#)]
36. Gražulis, S.; Daškevič, A.; Merkys, A.; Chateigner, D.; Lutterotti, L.; Quirós, M.; Serebryanaya, N.R.; Moeck, P.; Downs, R.T.; Le Bail, A. Crystallography Open Database (COD): An open-access collection of crystal structures and platform for world-wide collaboration. *Nucleic Acids Res.* **2012**, *40*, D420-7. [[CrossRef](#)]
37. Silva, R.S.; Cunha, F.; Barrozo, P. Raman spectroscopy of the Al-doping induced structural phase transition in LaCrO₃ perovskite. *Solid State Commun.* **2021**, *333*, 114346. [[CrossRef](#)]
38. Buscaglia, M.T.; Buscaglia, V.; Viviani, M.; Nanni, P.; Hanuskova, M. Influence of foreign ions on the crystal structure of BaTiO₃. *J. Eur. Ceram. Soc.* **2000**, *20*, 1997–2007. [[CrossRef](#)]
39. Khedhri, M.H.; Abdelmoula, N.; Khemakhem, H.; Douali, R.; Dubois, F. Structural, spectroscopic and dielectric properties of Ca-doped BaTiO₃. *Appl. Phys. A Mater. Sci. Process.* **2019**, *125*, 193. [[CrossRef](#)]
40. El Ghandouri, A.; Sayouri, S.; Lamcharfi, T.; Elbasset, A. Structural, microstructural and dielectric properties of Ba_{1-x}La_xTi_(1-x/4)O₃ prepared by sol gel method. *J. Adv. Dielect.* **2019**, *9*, 1950026. [[CrossRef](#)]
41. Da Lu, Y.; Han, D.D.; Liu, Q.L.; Wang, Y.D.; Sun, X.Y. Structure and Dielectric Properties of Ce and Ca Co-Doped BaTiO₃ Ceramics. *Key Eng. Mater.* **2016**, *680*, 184–188. [[CrossRef](#)]
42. Ren, P.; Wang, Q.; Wang, X.; Wang, L.; Wang, J.; Fan, H.; Zhao, G. Effects of doping sites on electrical properties of yttrium doped BaTiO₃. *Mater. Lett.* **2016**, *174*, 197–200. [[CrossRef](#)]
43. Rached, A.; Wederni, M.A.; Belkahla, A.; Dhahri, J.; Khirouni, K.; Alaya, S.; Martín-Palma, R.J. Effect of doping in the physico-chemical properties of BaTiO₃ ceramics. *Phys. B Condens. Matter* **2020**, *596*, 412343. [[CrossRef](#)]
44. Yen, F.-S.; Hsiang, H.-I.; Chang, Y.-H. Cubic to Tetragonal Phase Transformation of Ultrafine BaTiO₃ Crystallites at Room Temperature. *Jpn. J. Appl. Phys.* **1995**, *34*, 6149. [[CrossRef](#)]
45. Hayashi, H.; Nakamura, T.; Ebina, T. In-situ Raman spectroscopy of BaTiO₃ particles for tetragonal–cubic transformation. *J. Phys. Chem. Solids* **2013**, *74*, 957–962. [[CrossRef](#)]
46. He, Q.; Tang, X.; Zhang, J.; Wu, M. Raman study for BaTiO₃ system doped with various concentrations and treated at different temperatures. *Nanostructured Mater.* **1999**, *11*, 287–293. [[CrossRef](#)]
47. Yu, J.; Meng, X.J.; Sun, J.L.; Wang, G.S.; Chu, J.H. Phase transformation and Raman spectra in BaTiO₃ nanocrystals. *MRS Proc.* **2002**, *718*, D10-7. [[CrossRef](#)]
48. Shu, C.; Reed, D.; Button, T.W. A phase diagram of Ba_{1-x}Ca_xTiO₃ (x = 0–0.30) piezoceramics by Raman spectroscopy. *J. Am. Ceram. Soc.* **2018**, *101*, 2589–2593. [[CrossRef](#)]
49. Kappadan, S.; Gebreab, T.W.; Thomas, S.; Kalarikkal, N. Tetragonal BaTiO₃ nanoparticles: An efficient photocatalyst for the degradation of organic pollutants. *Mater. Sci. Semicond. Process.* **2016**, *51*, 42–47. [[CrossRef](#)]
50. Del López, M.C.B.; Fourlaris, G.; Rand, B.; Riley, F.L. Characterization of Barium Titanate Powders: Barium Carbonate Identification. *J. Am. Ceram. Soc.* **1999**, *82*, 1777–1786. [[CrossRef](#)]
51. Ravanamma, R.; Muralidhara Reddy, K.; Venkata Krishnaiah, K.; Ravi, N. Structure and morphology of yttrium doped barium titanate ceramics for multi-layer capacitor applications. *Mater. Today Proc.* **2021**, *46*, 259–262. [[CrossRef](#)]
52. Lin, F.; Jiang, D.; Ma, X.; Shi, W. Influence of doping concentration on room-temperature ferromagnetism for Fe-doped BaTiO₃ ceramics. *J. Magn. Magn. Mater.* **2008**, *320*, 691–694. [[CrossRef](#)]
53. Jin, X.; Sun, D.; Zhang, M.; Zhu, Y.; Qian, J. Investigation on FTIR spectra of barium calcium titanate ceramics. *J. Electroceram* **2009**, *22*, 285–290. [[CrossRef](#)]
54. Yang, F.; Yang, L.; Ai, C.; Xie, P.; Lin, S.; Wang, C.-Z.; Lu, X. Tailoring Bandgap of Perovskite BaTiO₃ by Transition Metals Co-Doping for Visible-Light Photoelectrical Applications: A First-Principles Study. *Nanomaterials* **2018**, *8*, 455. [[CrossRef](#)] [[PubMed](#)]
55. Tian, M.; Han, A.; Ma, S.; Zhu, X.; Ye, M.; Chen, X. Preparation of Cr-doped BaTiO₃ near infrared reflection pigment powder and its anti-aging performance for acrylonitrile-styrene-acrylate. *Powder Technol.* **2021**, *378*, 182–190. [[CrossRef](#)]
56. Eden, S.; Kapphan, S.; Hesse, H.; Trepakov, V.; Vikhnin, V.; Gregora, I.; Jastrabik, L.; Seglins, J. Observations of the absorption, infra-red emission, and excitation spectra of Cr in. *J. Phys. Condens. Matter* **1998**, *10*, 10775–10786. [[CrossRef](#)]

57. Orhan, E.; Pontes, F.M.; Pinheiro, C.D.; Longo, E.; Pizani, P.S.; Varela, J.A.; Leite, E.R.; Boschi, T.M.; Beltrán, A.; Andrés, J. Theoretical and experimental study of the relation between photoluminescence and structural disorder in barium and strontium titanate thin films. *J. Eur. Ceram. Soc.* **2005**, *25*, 2337–2340. [[CrossRef](#)]
58. Wang, Y.; Zhou, Q.; Zhang, Q.; Ren, Y.; Cui, K.; Cheng, C.; Wu, K. Effects of La-N Co-Doping of BaTiO₃ on Its Electron-Optical Properties for Photocatalysis: A DFT Study. *Molecules* **2024**, *29*, 2250. [[CrossRef](#)]
59. Rahman, M.A.; Hasan, Z.; Islam, J.; Das, D.K.; Chowdhury, F.I.; Khandaker, M.U.; Zayed, H.M.; Bradley, D.A.; Osman, H.; Ullah, M.H. Tailoring the Properties of Bulk BaTiO₃ Based Perovskites by Heteroatom-Doping towards Multifunctional Applications: A Review. *ECS J. Solid State Sci. Technol.* **2023**, *12*, 103015. [[CrossRef](#)]
60. *Perovskite Metal Oxides*; Elsevier: Amsterdam, The Netherlands, 2023; ISBN 9780323995290.
61. Hsiang, H.-I.; Yen, F.-S.; Chang, Y.-H. Effects of doping with La and Mn on the crystallite growth and phase transition of BaTiO₃ powders. *J. Mater. Sci.* **1996**, *31*, 2417–2424. [[CrossRef](#)]
62. Li, L.; Guo, R.; Gao, J.; Liu, J.; Zhao, Z.; Sheng, X.; Fan, J.; Cui, F. Insight into mechanochemical destruction of PFOA by BaTiO₃: An electron-dominated reduction process. *J. Hazard. Mater.* **2023**, *450*, 131028. [[CrossRef](#)]
63. Sanullah, I.; Khan, H.N.; Sajjad, A.; Khan, S.; Sabri, A.N.; Naseem, S.; Riaz, S. Improved osteointegration response using high strength perovskite BaTiO₃ coatings prepared by chemical bath deposition. *J. Mech. Behav. Biomed. Mater.* **2023**, *138*, 105635. [[CrossRef](#)]
64. Boschetto, F.; Doan, H.N.; Phong Vo, P.; Zanicco, M.; Yamamoto, K.; Zhu, W.; Adachi, T.; Kinashi, K.; Marin, E.; Pezzotti, G. Bacteriostatic Behavior of PLA-BaTiO₃ Composite Fibers Synthesized by Centrifugal Spinning and Subjected to Aging Test. *Molecules* **2021**, *26*, 2918. [[CrossRef](#)] [[PubMed](#)]
65. Kumar, A.; Kumar, S.; Prajapat, M.; Prakash, C. Magnetodielectric properties of Cr³⁺ ions doped BaTiO₃ multiferroic ceramic. In Proceedings of the Nanoforum 2014, Rome, Italy, 22–25 September 2014; AIP Publishing LLC.: Melville, NY, USA, 2015; p. 140008.
66. Hossain, K.M.; Ahmad, S.; Mitro, S.K. Physical properties of chromium-doped barium titanate: Effects of chromium incorporation. *Phys. B Condens. Matter* **2022**, *626*, 413494. [[CrossRef](#)]

Disclaimer/Publisher’s Note: The statements, opinions and data contained in all publications are solely those of the individual author(s) and contributor(s) and not of MDPI and/or the editor(s). MDPI and/or the editor(s) disclaim responsibility for any injury to people or property resulting from any ideas, methods, instructions or products referred to in the content.